

1**Evaluation of autoconversion and accretion enhancement factors in GCM warm-rain**
2**parameterizations using ground-based measurements at the Azores**

3Peng Wu¹, *Baiké Xi¹, Xiquan Dong¹, and Zhibo Zhang²

4¹ Department of Hydrology and Atmospheric Sciences, The University of Arizona, Tucson,
5Arizona, USA

6² Physics Department, The University of Maryland, Baltimore County, Maryland, USA

7

8

9 Submitted to Atmospheric Chemistry and Physics (November 21, 2018)

10

11

12**Keywords:** MBL clouds, enhancement factors, autoconversion and accretion parameterizations

13

14

15

16

17

18* Corresponding author address: Dr. Baiké Xi, Department of Hydrology and Atmospheric
19Sciences, University of Arizona, 1133 E. James E. Rogers Way, Tucson, AZ 85721-0011.
20baikexi@email.arizona.edu; Phone: 520-626-8945

21 **Abstract**

22 A great challenge in climate modelling is how to parametrize sub-grid cloud processes, such
23 as autoconversion and accretion in warm rain formation. In this study, we use ground-based
24 observations and retrievals over the Azores to investigate the so-called enhancement factors,
25 E_{auto} and E_{accr} , which are often used in climate models to account for the influences of sub-grid
26 variances of cloud and precipitation water on the autoconversion and accretion processes. E_{auto}
27 and E_{accr} are computed for different equivalent model grid sizes. The calculated E_{auto} values
28 increases from 1.96 (30 km) to 3.2 (180 km), and the calculated E_{accr} values increase from 1.53
29 (30 km) to 1.76 (180 km). Comparing the prescribed enhancement factors in Morrison and
30 Gettleman (2008, MG08) to the observed ones, we found that a higher E_{auto} (3.2) at small grids
31 and lower E_{accr} (1.07) are used in MG08, which helps to explain why most of the GCMs
32 produce too frequent precipitation events but with too light precipitation intensity. The ratios
33 of rain to cloud water mixing ratio at $E_{accr}=1.07$ and $E_{accr}=2.0$ are 0.063 and 0.142, respectively,
34 from observations, further suggesting that the prescribed value of $E_{accr}=1.07$ used in MG08 is
35 too small to simulate correct precipitation intensity. Both E_{auto} and E_{accr} increase when the
36 boundary layer becomes less stable, and the values are larger in precipitating clouds
37 ($CLWP > 75 \text{ gm}^{-2}$) than those in nonprecipitating clouds ($CLWP < 75 \text{ gm}^{-2}$). Therefore, the
38 selection of E_{auto} and E_{accr} values in GCMs should be regime- and resolution- dependent.

39

40 **1. Introduction**

41 Due to their vast areal coverage (Warren et al., 1986, 1988; Hahn and Warren, 2007) and
42 strong radiative cooling effect (Hartmann et al., 1992; Chen et al., 2000), small changes in the
43 coverage or thickness of marine boundary layer (MBL) clouds could change the radiative
44 energy budget significantly (Hartmann and Short, 1980; Randall et al., 1984) or even offset the
45 radiative effects produced by increasing greenhouse gases (Slingo, 1990). The lifetime of MBL
46 clouds remains an issue in climate models (Yoo and Li, 2012; Jiang et al., 2012; Yoo et al.,
47 2013; Stanfield et al., 2014) and represents one of the largest uncertainties in predicting future
48 climate (Wielicki et al., 1995; Houghton et al., 2001; Bony and Dufresne, 2005).

49 MBL clouds frequently produce precipitation, mostly in the form of drizzle (Austin et al.,
50 1995; Wood, 2005a; Leon et al., 2008; Wood, 2012). A significant amount of drizzle is
51 evaporated before reaching the surface, for example, about ~76% over the Azores region in
52 Northeast Atlantic (Wu et al., 2015), which provides another water vapour source for MBL
53 clouds. Due to their pristine environment and their close vicinity to the surface, MBL clouds
54 and precipitation are especially sensitive to aerosol perturbations (Quaas et al., 2009;
55 Kooperman et al., 2012). Thus, accurate prediction of precipitation is essential in simulating
56 the global energy budget and in constraining aerosol indirect effects in climate projections.

57 Due to the coarse spatial resolutions of the general circulation model (GCM) grid, many
58 cloud processes cannot be adequately resolved and must be parameterized. For example, warm

59 rain parameterizations in most GCMs treat the condensed water as either cloud or rain from the
60 collision-coalescence process that is partitioned into autoconversion and accretion sub-
61 processes in model parameterizations (Kessler, 1969; Tripoli and Cotton, 1980; Beheng, 1994;
62 Khairoutdinov and Kogan, 2000; Liu and Daum, 2004). Autoconversion represents the process
63 that drizzle drops being formed through the condensation of cloud droplets and accretion
64 represents the process where rain drops grow by the coalescence of drizzle-sized drops with
65 cloud droplets. Autoconversion mainly accounts for precipitation initiation while accretion
66 primarily contributes to precipitation intensity. Autoconversion is often parameterized as
67 functions of cloud droplet number concentration (N_c) and cloud water mixing ratio (q_c), while
68 accretion depends on both cloud and rain water mixing ratios (q_c and q_r) (Kessler, 1969; Tripoli
69 and Cotton, 1980; Beheng, 1994; Khairoutdinov and Kogan, 2000; Liu and Daum, 2004;
70 Wood, 2005b). The majority of previous studies suggested that these two processes as power
71 law functions of cloud and precipitation properties (See section 2 for details).

72 In conventional GCMs, the lack of information on the sub-grid variances of cloud and
73 precipitation leads to the unavoidable use of the grid-mean quantities ($\overline{N_c}$, $\overline{q_c}$, and $\overline{q_r}$, where
74 overbar denotes grid mean, same below) in calculating autoconversion and accretion rates.
75 MBL cloud liquid water path (CLWP) distributions are often positive skewed (Wood and
76 Hartmann, 2006; Dong et al., 2014a and 2014b), that is, the mean value is greater than mode
77 value. Thus, the mean value only represents a relatively small portion of samples. Also, due to

78 the nonlinear nature of the relationships, the two processes depend significantly on the sub-
79 grid variability and co-variability of cloud and precipitation microphysical properties (Weber
80 and Quass, 2012; Boutle et al., 2014). In some GCMs, sub-grid scale variability is often ignored
81 or hard coded using constants to represent the variabilities under all meteorological conditions
82 and across the entire globe (Pincus and Klein, 2000; Morrison and Gettleman, 2008; Lebsock
83 et al., 2013). This could lead to systematic errors in precipitation rate simulations (Wood et al.,
84 2002; Larson et al., 2011; Lebsock et al., 2013; Boutle et al., 2014; Song et al., 2018), where
85 GCMs are found to produce too frequent but too light precipitation compared to observations
86 (Zhang et al., 2002; Jess, 2010; Stephens et al., 2010; Nam and Quaas, 2012; Song et al., 2018).
87 The bias is found to be smaller by using a probability density function (PDF) of cloud water to
88 represent the sub-grid scale variability in autoconversion parameterization (Beheng, 1994;
89 Zhang et al., 2002; Jess, 2010), or more complexly, by integrating the autoconversion rate over
90 a joint PDF of liquid water potential temperature, and total water mixing ratio (Cheng and Xu,
91 2009).

92 Process rate enhancement factors (E) are introduced when considering sub-grid scale
93 variability in parameterizing grid-mean processes and they should be parameterized as
94 functions of the PDFs of cloud and precipitation properties within a grid box (Morrison and
95 Gettleman, 2008; Lebsock et al., 2013; Boutle et al., 2014). However, these values in some
96 GCM parameterization schemes are prescribed as constants regardless of underlying surface

97 or meteorological conditions (Xie and Zhang, 2015). Boutle et al. (2014) used aircraft in situ
98 measurements and remote sensing techniques to develop a parameterization for cloud and rain,
99 in which not only consider the sub-grid variabilities under different grid scales, but also
100 consider the variation of cloud and rain fractions. The parameterization was found to reduce
101 precipitation estimation bias significantly. Hill et al. (2015) modified this parameterization and
102 developed a regime and cloud type dependent sub-grid parameterization, which was
103 implemented to the Met Office Unified Model by Walters et al. (2017) and found that the
104 radiation bias is reduced using the modified parameterization. Using ground-based
105 observations and retrievals, Xie and Zhang (2015) proposed a scale-aware cloud
106 inhomogeneity parameterization that they applied to the Community Earth System Model
107 (CESM) and found that it can recognize spatial scales without manual tuning and can be applied
108 to the entire globe. The inhomogeneity parameter is essential in calculating enhancement
109 factors and affect the conversion rate from cloud to rain liquid. Xie and Zhang (2015), however,
110 did not evaluate the validity of CESM simulations from their parameterization; the effect of N_c
111 variability or the effect of covariance of cloud and rain on accretion process was not assessed.
112 Most recently, Zhang et al. (2018) derived the sub-grid distribution of CLWP and N_c from the
113 MODIS cloud product. They also studied the implication of the sub-grid cloud property
114 variations for the autoconversion rate simulation, in particular the enhancement factor, in
115 GCMs. For the first time, the enhancement factor due to the sub-grid variation of N_c is derived

116 from satellite observation, and results reveal several regions downwind of biomass burning
117 aerosols (e.g., Gulf of Guinea, East Coast of South Africa), air pollution (i.e., Eastern China
118 Sea), and active volcanos (e.g., Kilauea Hawaii and Ambae Vanuatu), where the enhancement
119 factor due to N_c is comparable, or even larger than that due to CLWP. However, one limitation
120 of Zhang et al. (2018) is the use of passive remote sensing data only, which cannot distinguish
121 cloud and rain water.

122 Dong et al. (2014a and 2014b) and Wu et al. (2015) reported MBL cloud and rain properties
123 over the Azores and provided the possibility of calculating the enhancement factors using
124 ground-based observations and retrievals. A joint retrieval method to estimate q_c and q_r profiles
125 is proposed based on existing studies and is presented in Appendix A. Most of the calculations
126 and analyses in this study is based on Morrison and Gettleman (2008, MG08 hereafter) scheme.
127 The enhancement factors in several other schemes are also discussed and compared with the
128 observational results and the approach in this study can be repeated for other microphysics
129 schemes in GCMs. This manuscript is organized as follows: section 2 includes a summary of
130 the mathematical formulas from previous studies that can be used to calculate enhancement
131 factors. Ground-based observations and retrievals are introduced in Section 3. Section 4
132 presents results and discussions, followed by summary and conclusions in Section 5. The
133 retrieval method used in this study is in Appendix A.

134 2. Mathematical Background

135 Autoconversion and accretion rates in GCMs are usually parameterized as power law
136 equations (Tripoli and Cotton, 1980; Beheng, 1994; Khairoutdinov and Kogan, 2000; Liu and
137 Daum, 2004):

$$138 \left(\frac{\partial q_r}{\partial t} \right)_{auto} = A \bar{q}_c^{a1} \bar{N}_c^{a2}, \quad (1)$$

$$139 \left(\frac{\partial q_r}{\partial t} \right)_{accr} = B (\bar{q}_c \bar{q}_r)^b, \quad (2)$$

140 where A , $a1$, $a2$, B , and b are coefficients in different schemes listed in Table 1. The \bar{q}_c , \bar{q}_r ,
141 and \bar{N}_c are grid-mean cloud water mixing ratio, rain water mixing ratio, and droplet number
142 concentration, respectively. Because it is widely used in model parameterizations, the detailed
143 results from Khairoutdinov and Kogan (2000) parameterization that been used in MG08
144 scheme will be shown in Section 4 while a summary will be given for other schemes.

145 Ideally, the covariance between physical quantities should be considered in the calculation
146 of both processes. However, \bar{q}_c and \bar{N}_c in Eq. (1) are arguably not independently retrieved in
147 our retrieval method which will be introduced in this section and Appendix A. Thus we only
148 assess the individual roles of q_c and N_c sub-grid variations in determining autoconversion rate.
149 q_c and q_r , on the other hand, are retrieved from two independent algorithms as shown in Dong
150 et al. (2014a and 2014b), Wu et al. (2015) and Appendix A, we will assess the effect of cloud
151 and rain property covariance on accretion rate calculations.

152 In the sub-grid scale, the PDFs of q_c and N_c are assumed to follow a gamma distribution
 153 based on observational studies of optical depth in MBL clouds (Barker et al., 1996; Pincus et
 154 al., 1999; Wood and Hartmann, 2006):

$$155 \quad P(x) = \frac{\alpha^\nu}{\Gamma(\nu)} x^{\nu-1} e^{-\alpha x}, \quad (3)$$

156 where x represents q_c or N_c with grid-mean quantity \bar{q}_c or \bar{N}_c , represented by μ , $\alpha = \nu/\mu$ is the
 157 scale parameter, σ^2 is the relative variance of x (= variance divided by μ^2), $\nu = 1/\sigma^2$ is the
 158 shape parameter. ν is an indicator of cloud field homogeneity, with large values representing
 159 homogeneous and small values indicating inhomogeneous cloud field.

160 By integrating autoconversion rate, Eq. (1), over the grid-mean rate, Eq. (3), with respect
 161 to sub-grid scale variation of q_c and N_c , the autoconversion rate can be expressed as:

$$162 \quad \left(\frac{\partial q_r}{\partial t}\right)_{auto} = A \mu_{q_c}^{a1} \mu_{N_c}^{a2} \frac{\Gamma(\nu+a)}{\Gamma(\nu)\nu^a}, \quad (4)$$

163 where $a = a1$ or $a2$. Comparing Eq. (4) to Eq. (1), the autoconversion enhancement factor
 164 (E_{auto}) can be given with respect to q_c and N_c :

$$165 \quad E_{auto} = \frac{\Gamma(\nu+a)}{\Gamma(\nu)\nu^a}. \quad (5)$$

166 In addition to fitting the distributions of q_c and N_c , we also tried two other methods to
 167 calculate E_{auto} . The first is to integrate Eq. (1) over the actual PDFs from observed or retrieved
 168 parameters and the second is to fit a lognormal distribution for sub-grid variability like what
 169 has been done in other studies (e.g., Lebsock et al., 2013; Larson and Griffin, 2013). It is found

170 that all three methods get similar results. In this study, we use a gamma distribution that is
 171 consistent with MG08. Also note that, in the calculation of E_{auto} from \overline{N}_c , the negative exponent
 172 (-1.79) may cause singularity problems in Eq. (5). When this situation occurs, we do direct
 173 calculations by integrating the PDF of \overline{N}_c rather than using Eq. (5).

174 To account for the covariance of microphysical quantities in a model grid, it is difficult to
 175 apply bivariate gamma distribution due to its complex nature. In this study, the bivariate
 176 lognormal distribution of q_c and q_r is used (Lebsock et al., 2013; Boutle et al., 2014) and can
 177 be written as:

$$178 \quad P(\overline{q}_c, \overline{q}_r) = \frac{1}{2\pi\overline{q}_c\overline{q}_r\sigma_{q_c}\sigma_{q_r}\sqrt{1-\rho^2}} \exp\left\{-\frac{1}{2}\frac{1}{1-\rho^2}\left[\left(\frac{\ln\overline{q}_c-\mu_{q_c}}{\sigma_{q_c}}\right)^2 - 2\rho\left(\frac{\ln\overline{q}_c-\mu_{q_c}}{\sigma_{q_c}}\right)\left(\frac{\ln\overline{q}_r-\mu_{q_r}}{\sigma_{q_r}}\right) + \right.\right. \\ 179 \quad \left.\left.\left(\frac{\ln\overline{q}_r-\mu_{q_r}}{\sigma_{q_r}}\right)^2\right]\right\}, \quad (6)$$

180 where σ is standard deviation and ρ is the correlation coefficient of q_c and q_r .

181 Similarly, by integrating the accretion rate in Eq. (2) from Eq. (6), we get the accretion
 182 enhancement factor (E_{accr}) of:

$$183 \quad E_{accr} = \left(1 + \frac{1}{v_{q_c}}\right)^{\frac{1.15^2-1.15}{2}} \left(1 + \frac{1}{v_{q_r}}\right)^{\frac{1.15^2-1.15}{2}} \exp(\rho 1.15^2 \sqrt{\ln\left(1 + \frac{1}{v_{q_c}}\right) \ln\left(1 + \frac{1}{v_{q_r}}\right)}). \quad (7)$$

184 3. Ground-based observations and retrievals

185 The datasets used in this study were collected at the Department of Energy (DOE)
186 Atmospheric Radiation Measurement (ARM) Mobile Facility (AMF), which was deployed on
187 the northern coast of Graciosa Island (39.09°N, 28.03°W) from June 2009 to December 2010
188 (for more details, please refer to Rémillard et al., 2012; Dong et al., 2014a and Wood et al.,
189 2015). The detailed operational status of the remote sensing instruments on AMF was
190 summarized in Figure 1 of Rémillard et al. (2012) and discussed in Wood et al. (2015). The
191 ARM Eastern North Atlantic (ENA) site was established on the same island in 2013 and
192 provides long-term continuous observations.

193 The cloud-top heights (Z_{top}) were determined from W-band ARM cloud radar (WACR)
194 reflectivity and only single-layered low-level clouds with $Z_{\text{top}} \leq 3$ km are selected. Cloud-base
195 heights (Z_{base}) were detected by a laser ceilometer (CEIL) and the cloud thickness was simply
196 the difference between cloud top and base heights. The cloud liquid water path (CLWP) was
197 retrieved from microwave radiometer (MWR) brightness temperatures measured at 23.8 and
198 31.4 GHz using a statistical retrieval method with an uncertainty of 20 g m^{-2} for $\text{CLWP} < 200$
199 g m^{-2} , and 10% for $\text{CLWP} > 200 \text{ g m}^{-2}$ (Liljegren et al., 2001; Dong et al., 2000). Precipitating
200 status is identified through a combination of WACR reflectivity and Z_{base} . As in Wu et al.
201 (2015), we labelled the status of a specific time as “precipitating” if the WACR reflectivity
202 below the cloud base exceeds -37 dBZ.

203 The ARM merged sounding data have a 1-min temporal and 20-m vertical resolution below
204 3 km (Trojan, 2012). In this study, the merged sounding profiles are averaged to 5-min
205 resolution. Pressure and temperature profiles are used to calculate air density (ρ_{air}) profiles
206 and to infer adiabatic cloud water content.

207 Cloud droplet number concentration (N_c) is retrieved using the methods presented in Dong
208 et al. (1998, 2014a and 2014b) and are assumed to be constant in a cloud layer. Vertical profiles
209 of cloud and rain water content (CLWC and RLWC) are retrieved by combining WACR
210 reflectivity, CEIL attenuated backscatter and by assuming adiabatic growth of cloud parcels.
211 The detailed description is presented in Appendix A with the results from a selected case. The
212 CLWC and RLWC values are transformed to q_c and q_r by dividing by air density (e.g., $q_c(z) =$
213 $CLWC(z)/\rho_{air}(z)$).

214 The estimated uncertainties for the retrieved q_c and q_r are 30% and 18%, respectively (see
215 Appendix A). We used the estimated uncertainties of q_r and q_c as inputs of Eqs. (4) and (7) to
216 assess the uncertainties of E_{auto} and E_{accr} . For instance, $(1 \pm 0.3)q_c$ are used in Eq. (4) and the
217 mean differences are then used as the uncertainty of E_{auto} . Same method is used to estimate the
218 uncertainty for E_{accr} .

219 The autoconversion and accretion parameterizations partitioned from the collision-
220 coalescence process dominate at different levels in a cloud layer. Autoconversion dominates
221 around cloud top where cloud droplets reach maximum by condensation and accretion is

222 dominant at middle and lower parts of the cloud where rain drops sediment and continue to
223 grow by collecting cloud droplets. Complying with the physical processes, we estimate
224 autoconversion and accretion rates at different levels of a cloud layer in this study. The
225 averaged q_c within the top five range gates (~215 m thick) are used to calculate E_{auto} . To
226 calculate E_{accr} , we use the averaged q_c and q_r within five range gates around the maximum
227 radar reflectivity. If the maximum radar reflectivity appears at the cloud base, then five range
228 gates above the cloud base are used.

229 The ARM merged sounding data are also used to calculate lower tropospheric stability
230 ($LTS = \theta_{700 \text{ hPa}} - \theta_{1000 \text{ hPa}}$), which is used to infer the boundary layer stability. In this study,
231 unstable and stable boundary layers are defined as LTS less than 13.5 K and greater than 18 K,
232 respectively, and environment with an LTS between 13.5 K and 18 K is defined as mid-stable
233 (Wang et al. 2012; Bai et al. 2018). Enhancement factors in different boundary layers are
234 summarized in Section 4.2 and may be used as references for model simulations. Further, two
235 regimes are classified: CLWP greater than 75 g m^{-2} as precipitating and CLWP less than 75 g
236 m^{-2} as nonprecipitating (Rémillard et al., 2012).

237 To evaluate the dependence of autoconversion and accretion rates on sub-grid variabilities
238 for different model spatial resolutions, an averaged wind speed within a cloud layer was
239 extracted from merged sounding and used in sampling observations over certain periods to
240 mimic different grid sizes in GCMs. For example, two hours of observations corresponds to a

241 72-km horizontal equivalent grid box if mean in-cloud wind speed is 10 m s^{-1} horizontal wind
242 and if the wind speed is 5 m s^{-1} , four hours of observations is needed to mimic the same
243 horizontal equivalent grid. We used six horizontal equivalent grid sizes (30-, 60-, 90-, 120-,
244 150-, and 180-km) and mainly show the results from 60-km and 180-km horizontal equivalent
245 grid sizes in Section 4. For convenience, we refer ‘equivalent size’ as ‘horizontal equivalent
246 grid size’ from now on.

247 **4. Results and discussions**

248 In this section, we first show the data and methods using a selected case, followed by
249 statistical analysis based on 19 months of data and multiple time-intervals.

250 **4.1 Case study**

251 The selected case occurred on July 27, 2010 (Figure 1a) at the Azores. This case was
252 characterized by a long time of non-precipitating or light drizzling cloud development (00:00-
253 14:00 UTC) before intense drizzling occurred (14:00-20:00 UTC). Wu et al. (2017) studied
254 this case in detail to demonstrate the effect of wind shear on drizzle initiation. Here, we choose
255 two periods corresponding to a 180-km equivalent size and having similar mean q_c near cloud
256 top: 0.28 g kg^{-1} for period c and 0.26 g kg^{-1} for period d but with different distributions (Figures
257 1c and 1d). The PDFs of q_c are then fitted using gamma distributions to get shape parameters
258 (ν) as shown in Figures 1c and 1d. Smaller ν is usually associated with a more inhomogeneous
259 cloud field, which allows more rapid drizzle production and more efficient liquid

260 transformation from cloud to rain (Xie and Zhang, 2015) in regions that satisfy precipitation
261 criteria, which is usually controlled using threshold q_r , droplet size or relative humidity
262 (Kessler, 1969; Liu and Daum, 2004). The period d has a wider q_c distribution than the period
263 c, resulting in a smaller ν and thus larger E_{auto} . Using the fitted ν , the E_{auto} from q_c is calculated
264 from Eq. (5) and the period d is larger than the period c (1.80 vs. 1.33). The E_{auto} values for the
265 periods d and c can also be calculated from N_c using the same procedure as q_c with a similar
266 result (2.1 vs. 1.51). The E_{accr} values for the periods d and c can be calculated from the
267 covariance of q_c and q_r and Eq. (7). Not surprisingly, the period d has larger E_{accr} than the
268 period c. The combination of larger E_{auto} and E_{accr} in the period d contributes to the rapid drizzle
269 production and high rain rate as seen from WACR reflectivity and q_r in Figure A1.

270 It is important to understand the physical meaning of enhancement factors in precipitation
271 parameterization. For example, if we assume two scenarios for q_c with a model grid having the
272 same mean values but different distributions: (1) The distribution is extremely homogeneous,
273 there will be no sub-grid variability because the cloud has the same chance to precipitate and
274 the enhancement factors would be unity (this is true for arbitrary grid-mean q_c amount as well).
275 (2) The cloud field gets more and more inhomogeneous with a broad range of q_c within the
276 model grid box, which results in a greater enhancement factor and increases the possibility of
277 precipitation. That is, a large enhancement factor can make the part of the cloud with higher q_c

278 within the grid box become more efficient in generating precipitation, rather than the entire
279 model grid.

280 Using the LWP retrieved from the Moderate Resolution Imaging Spectroradiometer
281 (MODIS) as an indicator of cloud inhomogeneous, Wood and Hartmann (2006) found that
282 when clouds become more inhomogeneous, cloud fraction decreases, and open cells become
283 dominant with stronger drizzling process (Comstock et al., 2007). The relationship between
284 reduced homogeneity and stronger precipitation intensity is found in this study, which is similar
285 to the findings in other studies (e.g., Wood and Hartmann, 2006, Comstock et., 2007, Barker
286 et al., 1996; Pincus et al., 1999).

287 It is clear that q_c and N_c in Figure 1b are correlated with each other. In addition to their
288 natural relationships, q_c and N_c in our retrieval method are also correlated (Dong et al., 2014a
289 and 2014b). Thus, the effect of q_c and N_c covariance on E_{auto} is not included in this study. In
290 Figures 1c and 1d, the results are calculated using equivalent size of 180-km for the selected
291 case on 27 July 2010. In Section 4.2, we will use these approaches to calculate their statistical
292 results for multiple equivalent sizes using the 19-month ARM ground-based observations and
293 retrievals.

294 **4.2 Statistical result**

295 For a specific equivalent size, e.g. 60-km, we estimate the shape parameter (ν) and calculate
296 E_{auto} through Eqns. (5) and (7). The PDFs of E_{auto} for both 60-km and 180-km equivalent sizes

297 are shown in Figures 2a-2d. The distributions of E_{auto} values calculated from q_c with 60-km
298 and 180-km equivalent sizes (Figures 2a and 2b) are different to each other (2.79 vs. 3.3). The
299 calculated E_{auto} values range from 1 to 10, and most are less than 4. The average value for the
300 60-km equivalent size (2.79) is smaller than that for the 180-km equivalent size (3.2), indicating
301 a possible dependence of E_{auto} on model grid size. Because drizzle-sized drops are primarily
302 resulted from the autoconversion, we investigate the relationship between E_{auto} and
303 precipitation frequency, which is defined as the average percentage of drizzling occurrence
304 based on radar reflectivity below the cloud base. Given the average LWP at Azores from Dong
305 et al. (2014b, 109-140 g m⁻²), the precipitation frequency (black lines in Figures 2a and 2b)
306 agrees well with those from Kubar et al. (2009, 0.1-0.7 from their Figure 11). The precipitation
307 frequency within each bin shows an increasing trend for E_{auto} from 0 to 4-6, then oscillates
308 when $E_{auto} > 6$, indicating that in precipitation initiation process, E_{auto} keeps increasing to a
309 certain value (~6) until the precipitation frequency reaches a near-steady state. Larger E_{auto}
310 values do not necessarily result in higher precipitation frequency but instead may produce more
311 drizzle-sized drops from autoconversion process when the cloud is precipitating.

312 The PDFs of E_{auto} calculated from N_c also share similar patterns of positive skewness and
313 peaks at ~1.5-2.0 for the 60-km and 180-km equivalent sizes (Figures 2c and 2d). Although the
314 average values are close to their q_c counterparts (2.54 vs. 2.79 for 60-km and 3.45 vs. 3.2 for
315 180-km), the difference in E_{auto} between 60-km and 180-km equivalent sizes becomes large.

316 The precipitation frequencies within each bin are nearly constant or slightly decrease, which
317 are different to their q_c counterparts shown in Figures 2a and 2b. This suggests complicated
318 effects of droplet number concentration on precipitation initiation and warrants more
319 explorations of aerosol-cloud-precipitation interactions. As mentioned in Section 2, q_c and N_c
320 are also fitted using lognormal distributions to calculate E_{auto} , those are close to the results in
321 Figure 2 (not shown here) with average values of 3.28 and 3.84, respectively, for 60-km and
322 180-km equivalent sizes. Because the E_{auto} values calculated from q_c and N_c are close to each
323 other, we will focus on analyzing the results from q_c only for simplicity and clarity. The effect
324 of q_c and N_c covariance, as stated in Section 4.1, is not presented in this study due to the intrinsic
325 correlation in the retrieval (Dong et al., 2014a and 2014b and Appendix A of this study).

326 The covariance of q_c and q_r is included in calculating E_{accr} and the results are shown in
327 Figures 2e and 2f. The calculated E_{accr} values range from 1 to 4 with mean values of 1.62 and
328 1.76 for 60-km and 180-km equivalent sizes, respectively. These two mean values are much
329 greater than the prescribed value used in MG08 (1.07). Since accretion is dominant at middle
330 and lower parts of the cloud where rain drops sediment and continue to grow by collecting
331 cloud droplets, we superimpose the ratio of q_r to q_c within each bin (black lines in Figures 2e
332 and 2f) to represent the portion of rain water in the cloud layer. In both panels, the ratios are
333 less than 15%, which means that q_r can be one order of magnitude smaller than q_c . The
334 differences in magnitude are consistent with previous CloudSat and aircraft results (e.g., Boutle

335 et al., 2014). This ratio increases from $E_{accr}=0$ to ~ 2 , and then decreases, suggesting a possible
336 optimal state for the collision-coalescence process to achieve maximum efficiency for
337 converting cloud water into rain water at $E_{accr}=2$. In other words, the conversion efficiency
338 cannot be infinitely increased with E_{accr} under available cloud water. The ratio of q_r to q_c
339 increases from $E_{accr}=1.07$ (0.063) to $E_{accr}=2.0$ (0.142), indicating that the fraction of rain water
340 in total water using the prescribed E_{accr} is too low. This ratio could be increased significantly
341 using a large E_{accr} value, therefore increasing precipitation intensity in the models. This further
342 proves that the prescribed value of $E_{accr}=1.07$ used in MG08 is too small to correctly simulate
343 precipitation intensity in the models. Therefore, similar to the conclusions in Lebsock et al.
344 (2013) and Boutle et al. (2014), we suggest increasing E_{accr} from 1.07 to 1.5-2.0 in GCMs.

345 To illustrate the impact of using prescribed enhancement factors, autoconversion and
346 accretion rates are calculated using the prescribed values (e.g., 3.2 for E_{auto} and 1.07 for E_{accr} ,
347 MG08; Xie and Zhang, 2015) and the newly calculated ones in Figure 2 that use observations
348 and retrievals. Figure 3 shows the joint density of autoconversion (Figures 3a and 3b) and
349 accretion rates (Figures 3c and 3d) from observations (x-axis) and model parameterizations (y-
350 axis) for 60-km and 180-km equivalent sizes. Despite the spread, the peaks of the joint density
351 of autoconversion rate appear slightly above the one-to-one line especially for the 60-km
352 equivalent size, suggesting that cloud droplets in the model are more easily to be converted
353 into drizzle/rain drops than observations. On the other hand, the peaks of accretion rate appear

354 slightly below the one-to-one line which indicates that simulated precipitation intensities are
355 lower than observed ones. The magnitudes of the two rates are consistent with Khairoutdinov
356 and Kogan (2000), Liu and Daum (2004), and Wood (2005b).

357 Compared to the observations, the precipitation in GCMs occurs at higher frequencies with
358 lower intensities, which might explain why the total precipitation amounts are close to surface
359 measurements over an entire grid box. This ‘promising’ result, however, fails to simulate
360 precipitation on the right scale and cannot capture the correct rain water amount, thus providing
361 limited information in estimating rain water evaporation and air-sea energy exchange.

362 Clouds in an unstable boundary layer have a better chance of getting moisture supply from
363 the surface by upward motion than clouds in a stable boundary layer. Precipitation frequencies
364 are thus different in these two boundary layer regimes. For example, clouds in a relatively
365 unstable boundary layer more easily produce drizzle than those in a stable boundary layer (Wu
366 et al., 2017). Provided the same boundary layer condition, CLWP is an important factor in
367 determining the precipitation status of clouds. At the Azores, precipitating clouds are more
368 likely to have CLWP greater than 75 g m^{-2} than their nonprecipitating counterparts (Rémillard
369 et al., 2012). To further investigate what conditions and parameters can significantly influence
370 the enhancement factors, we classify low-level clouds according to their boundary layer
371 conditions and CLWPs.

372 The averaged E_{auto} and E_{accr} values for each category are listed in Table 2. Both E_{auto} and
373 E_{accr} increase when the boundary layer becomes less stable, and these values become larger in
374 precipitating clouds ($CLWP > 75 \text{ gm}^{-2}$) than those in nonprecipitating clouds ($CLWP < 75 \text{ gm}^{-2}$).
375 In real applications, autoconversion process only occurs when q_c or cloud droplet size reaches
376 a certain threshold (e.g., Kessler, 1969 and Liu and Daum, 2004). Thus, it will not affect model
377 simulations if a valid E_{auto} is assigned to Eq. (1) in a nonprecipitating cloud. The E_{auto} values
378 in both stable and mid-stable boundary layer conditions are smaller than the prescribed value
379 of 3.2, while the values in unstable boundary layers are significantly larger than 3.2 regardless
380 of if they are precipitating or not. All E_{accr} values are greater than the constant of 1.07. The
381 E_{auto} values in Table 2 range from 2.32 to 6.94 and the E_{accr} values vary from 1.42 to 1.86,
382 depending on different boundary layer conditions and CLWPs. Therefore, as suggested by Hill
383 et al. (2015), the selection of E_{auto} and E_{accr} values in GCMs should be regime-dependent.

384 To properly parameterize sub-grid variabilities, the approaches by Hill et al. (2015) and
385 Walters et al. (2017) can be adopted. To use MG08 and other parameterizations in GCMs as
386 listed in Table 1, proper adjustments can be made according to the model grid size, boundary
387 layer conditions, and precipitating status. As stated in the methodology, we used a variety of
388 equivalent sizes. Figure 4 demonstrates the dependence of both enhancement factors on
389 different model grid sizes. The E_{auto} values (red line) increase from 1.97 at an equivalent size
390 of 30 km to 3.15 at an equivalent size of 120 km, which are 38.4% and 2% percent lower than

391 the prescribed value (3.2, upper dashed line). After that, the E_{auto} values remain relatively
392 constant of ~ 3.18 when the equivalent model size is 180 km, which is close to the prescribed
393 value of 3.2 used in MG08. This result indicates that the prescribed value in MG08 represents
394 well in large grid sizes in GCMs. The E_{accr} values (blue line) increase from 1.53 at an equivalent
395 size of 30 km to 1.76 at an equivalent size of 180 km, those are 43% and 64%, respectively,
396 larger than the prescribed value (1.07, lower dashed line). The shaded areas represent the
397 uncertainties of E_{auto} and E_{accr} associated with the uncertainties of the retrieved q_c and q_r . When
398 equivalent size increases, the uncertainties slightly decrease. The prescribed E_{auto} is close to
399 the upper boundary of uncertainties except for the 30-km equivalent size, while the prescribed
400 E_{accr} is significantly lower than the lower boundary.

401 It is noted that E_{auto} and E_{accr} depart from their prescribed values at opposite directions as
402 the equivalent size increases. For models with finer resolutions (e.g., 30-km), both E_{auto} and
403 E_{accr} are significantly different from the prescribed values, which can partially explain the issue
404 of ‘too frequent’ and ‘too light’ precipitation. Under both conditions, the accuracy of
405 precipitation estimation is degraded. For models with coarser resolutions (e.g., 180-km),
406 average E_{auto} is exactly 3.2 while E_{accr} is much larger than 1.07 when compared to finer
407 resolution simulations. In such situations, the simulated precipitation will be dominated by the
408 ‘too light’ problem, in addition to regime-dependent (Table 2) and as in Xie and Zhang (2015),
409 E_{auto} and E_{accr} should be also scale-dependent.

410 Also note that the location of ground-based observations and retrievals used in this study is
411 on the remote ocean where the MBL clouds mainly form in a relatively stable boundary layer
412 and are characterized by high precipitation frequency. Even in such environments, however,
413 the GCMs overestimate the precipitation frequency (Ahlgrimm and Forbes, 2014).

414 To further investigate how enhancement factors affect precipitation simulations, we use
415 E_{auto} as a fixed value of 3.2 in Eq. (4), and then calculate the q_c needed for models to reach the
416 same autoconversion rate as observations. The q_c differences between models and observations
417 are then calculated, which represent the q_c adjustment in models to get a realistic
418 autoconversion rate in the simulations. Similar to Figure 1, the PDFs of q_c differences (model
419 – observation) are plotted in Figures 5a and 5b for 60-km and 180-km equivalent sizes. Figure
420 5c shows the average percentages of model q_c adjustments for different equivalent sizes. The
421 mode and average values for 30-km equivalent size is negative, suggesting that models need to
422 simulate lower q_c in general to get reasonable autoconversion rates. Lower q_c values are usually
423 associated with smaller E_{auto} values that induce lower simulated precipitation frequency. On
424 average, the percentage of q_c adjustments decrease with increasing equivalent size. For
425 example, the adjustments for finer resolutions (e.g., 30-60 km) can be ~20% of the q_c , whereas
426 adjustments in coarse resolution models (e.g., 120 – 180 km) are relatively small because the
427 prescribed E_{auto} (=3.2) is close to the observed ones (Figure 4) and when equivalent size is 180-
428 km, no adjustment is needed. The adjustment method presented in Figure 5, however, may

429 change cloud water substantially and may cause a variety of subsequent issues, such as altering
430 cloud radiative effects and disrupting the hydrological cycle. The assessment in Figure 5 only
431 provides a reference to the equivalent effect on cloud water by using the prescribed E_{auto} value
432 as compared to those from observations.

433 All above discussions are based on the prescribed E_{auto} and E_{accr} values (3.2 and 1.07) in
434 MG08. Whereas there are quite a few parameterizations that have been published so far. In this
435 study, we list E_{auto} and E_{accr} for three other widely used parameterization schemes in Table 3,
436 which are given only for 60-km and 180-km equivalent sizes. The values of the exponent in
437 each scheme directly affect the values of the enhancement factors. For example, the scheme in
438 Beheng (1994) has highest degree of nonlinearity and hence has the largest enhancement
439 factors. The scheme in Liu and Daum (2004) is very similar to the scheme in Khairoutdinov
440 and Kogan (2000) because both schemes have a physically realistic dependence on cloud water
441 content and number concentration (Wood, 2005b). For a detailed overview and discussion of
442 various existing parameterizations, please refer to Liu and Daum (2004), Liu et al. (2006a), Liu
443 et al. (2004b), Wood (2005b) and Michibata and Takemura (2015). A physical based
444 autoconversion parameterization was developed by Lee and Baik (2017) in which the scheme
445 was derived by solving stochastic collection equation with an approximated collection kernel
446 that is constructed using the terminal velocity of cloud droplets and the collision efficiency
447 obtained from a particle trajectory model. Due to the greatly increased complexity of their

448 equation, we do not attempt to calculate E_{auto} here but should be examined in future studies due
449 to the physics feasibility of the Lee and Baik (2017) scheme.

450

451 **5. Summary**

452 To better understand the influence of sub-grid cloud variations on the warm-rain process
453 simulations in GCMs, we investigated the warm-rain parameterizations of autoconversion
454 (E_{auto}) and accretion (E_{accr}) enhancement factors in MG08. These two factors represent the
455 effects of sub-grid cloud and precipitation variabilities when parameterizing autoconversion
456 and accretion rates as functions of grid-mean quantities. E_{auto} and E_{accr} are prescribed as 3.2
457 and 1.07, respectively, in the widely used MG08 scheme. To assess the dependence of the two
458 parameters on sub-grid scale variabilities, we used ground-based observations and retrievals
459 collected at the DOE ARM Azores site to reconstruct the two enhancement factors in different
460 equivalent sizes.

461 From the retrieved q_c and q_r profiles, the averaged q_c within the top five range gates are
462 used to calculate E_{auto} and the averaged q_c and q_r within five range gates around maximum
463 reflectivity are used to calculate E_{accr} . The calculated E_{auto} values from observations and
464 retrievals increase from 1.96 at an equivalent size of 30 km to 3.18 at an equivalent size of 150
465 km. These values are 38% and 0.625% lower than the prescribed value of 3.2. The prescribed
466 value in MG08 represents well in large grid sizes in GCMs (e.g., 180^2 km² grid). On the other

467 hand, the E_{accr} values increase from 1.53 at an equivalent size of 30 km to 1.76 at an equivalent
468 size of 180 km, which are 43% and 64% higher than the prescribed value (1.07). The higher
469 E_{auto} and lower E_{accr} prescribed in GCMs help to explain the issue of too frequent precipitation
470 events with too light precipitation intensity. The ratios of rain to cloud liquid water increase
471 with increasing E_{accr} from 0 to 2, and then decrease after that, suggesting a possible optimal
472 state for the collision-coalescence process to achieve maximum efficiency for converting cloud
473 water into rain water at $E_{accr}=2$. The ratios of q_r to q_c at $E_{accr}=1.07$ and $E_{accr}=2.0$ are 0.063 and
474 0.142, further proving that the prescribed value of $E_{accr}=1.07$ is too small to simulate correct
475 precipitation intensity in models.

476 To further investigate what conditions and parameters can significantly influence the
477 enhancement factors, we classified low-level clouds according to their boundary layer
478 conditions and CLWPs. Both E_{auto} and E_{accr} increase when the boundary layer conditions
479 become less stable, and the values are larger in precipitating clouds ($CLWP > 75 \text{ gm}^{-2}$) than
480 those in nonprecipitating clouds ($CLWP < 75 \text{ gm}^{-2}$). The E_{auto} values in both stable and mid-stable
481 boundary layer conditions are smaller than the prescribed value of 3.2, while those in unstable
482 boundary layers conditions are significantly larger than 3.2 regardless of whether or not the
483 cloud is precipitating (Table 2). All E_{accr} values are greater than the prescribed value of 1.07.
484 Therefore, the selection of E_{auto} and E_{accr} values in GCMs should be regime-dependent, which
485 also has been suggested by Hill et al. (2015) and Walters et al. (2017).

486 This study, however, did not include the effect of uncertainties in GCM simulated cloud
487 and precipitation properties on sub-grid scale variations. For example, we did not consider the
488 behavior of the two enhancement factors under different aerosol regimes, a condition which
489 may affect precipitation formation process. The effect of aerosol-cloud-precipitation-
490 interactions on cloud and precipitation sub-grid variabilities may be of comparable importance
491 to meteorological regimes and precipitation status and deserves a further study. Other than the
492 large-scale dynamics, e.g., LTS in this study, upward/downward motion in sub-grid scale may
493 also modify cloud and precipitation development and affect the calculations of enhancement
494 factors. The investigation of the dependence of E_{auto} and E_{accr} on aerosol type and concentration
495 as well as on vertical velocity would be a natural extension and complement of current study.
496 In addition, other factors may also affect precipitation frequency and intensity even under the
497 same aerosol regimes and even if the clouds have similar cloud water contents. Wind shear, for
498 example as presented in Wu et al. (2017), is an external variable that can affect precipitation
499 formation. Further studies are needed to evaluate the role of the covariance of q_c and N_c in sub-
500 grid scales on E_{auto} determinations, which is beyond the scope of this study and requires
501 independent retrieval techniques.

502

503 **Appendix A: Joint cloud and rain LWC profile estimation**

504 If a time step is identified as non-precipitating, the cloud liquid water content (CLWC)
505 profile is retrieved using Frisch et al. (1995) and Dong et al. (1998, 2014a and 2014b). The
506 retrieved CLWC is proportional to radar reflectivity.

507 If a time step is identified as precipitating (maximum reflectivity below cloud base
508 exceeds -37 dBZ), CLWC profile is first inferred from temperature and pressure in merged
509 sounding by assuming adiabatic growth. Marine stratocumulus is close to adiabatic (Albrecht
510 et al. 1990) and was used in cloud property retrievals in literature (e.g., Rémillard et al., 2013).
511 In this study, we use the information from rain properties near cloud base to further constrain
512 the adiabatic CLWC ($CLWC_{adiabatic}$).

513 Adopting the method of O'Connor et al. (2005), Wu et al. (2015) retrieved rain properties
514 below cloud base (CB) for the same period as in this study. In Wu et al. (2015), rain drop size
515 (median diameter, D_0), shape parameter (μ), and normalized rain droplet number concentration
516 (N_W) are retrieved for the assumed rain particle size distribution (PSD):

$$517 \quad n_r(D) = N_W f(\mu) \left(\frac{D}{D_0}\right)^\mu \exp\left[-\frac{(3.67+\mu)D}{D_0}\right] \quad (\text{A1})$$

518 To infer rain properties above cloud base, we adopt the assumption in Fielding et al. (2015)
519 that N_W increases from below CB to within the cloud. This assumption is consistent with the *in*
520 *situ* measurement in Wood (2005a). Similar as Fielding et al. (2015), we use constant N_W within
521 cloud if the vertical gradient of N_W is negative below CB. The μ within cloud is treated as

522 constant and is taken as the averaged value from four range gates below CB. Another
 523 assumption in the retrieval is that the evaporation of rain drops is negligible from one range
 524 gate above CB to one range gate below CB thus we assume rain drop size is the same at the
 525 range gate below and above CB.

526 With the above information, we can calculate the reflectivity contributed by rain at the first
 527 range gate above CB ($Z_r(1)$) and the cloud reflectivity ($Z_c(1)$) is then $Z_c(1) = Z(1) - Z_r(1)$,
 528 where $Z(1)$ is WACR measured reflectivity at first range gate above CB. Using cloud droplet
 529 number concentration (N_c) from Dong et al. (2014a and 2014b), CLWC at the first range gate
 530 above CB can be calculated through

$$531 \quad Z_c(1) = 2^6 \int_0^\infty n_c(r) r^6 dr = \frac{36}{\pi^2 \rho_w^2} \frac{CLWC(1)_{reflectivity}^2}{N_c} \exp(9\sigma_x^2) \quad (A2.1)$$

$$532 \quad CLWC(1)_{reflectivity} = \sqrt{\frac{Z_c(1) \pi^2 \rho_w^2 N_c}{36 \exp(9\sigma_x^2)}} \quad (A2.2)$$

533 Where ρ_w is liquid water density $n_c(r)$ is lognormal distribution of cloud PSD with
 534 logarithmic width σ_x . Geoffroy et al. (2010) suggested that σ_x increases with the length scale
 535 and Witte et al. (2018) showed that σ_x also dependent on the choice instrumentation. The
 536 variations of σ_x should be reflected in the retrieval by using different σ_x values with time.
 537 However, no aircraft measurements were available during CAP-MBL to provide σ_x over the
 538 Azores region. The inclusion of solving σ_x in the retrieval adds another degree of freedom to
 539 the equations and complicates the problem considerably. In this study, σ_x is set to a constant

540 value of 0.38 from Miles et al. (2000), which is a statistical value from aircraft measurements
541 of marine low-level clouds.

542 We then compare the $CLWC_{adiabatic}$ and the one calculated from $CLWC_{reflectivity}$ at the
543 first range gate above CB. A scale parameter (s) is defined as $s = \frac{CLWC_{reflectivity}(1)}{CLWC_{adiabatic}(1)}$ and the
544 entire profile of $CLWC_{adiabatic}$ is multiplied by s to correct the bias from cloud sub-
545 adiabaticity. Reflectivity profile from cloud is then calculated from Eq. (A2.1) using the
546 updated $CLWC_{adiabatic}$ and the remaining reflectivity profile from WACR observation is
547 regarded as rain contribution. Rain particle size can then be calculated given that N_W and μ are
548 known and rain liquid water content (RLWC) can be estimated.

549 There are two constrains used in the retrieval. One is that the summation of cloud and rain
550 liquid water path (CLWP and RLWP) must be equal to the LWP from microwave radiometer
551 observation. Another is that rain drop size (D_0) near cloud top must be equal or greater than 50
552 μm and if D_0 is less than 50 μm , we decrease N_W for the entire rain profile within cloud and
553 repeat the calculation until the 50 μm criteria is satisfied.

554 It is difficult to quantitatively estimate the retrieval uncertainties without aircraft in situ
555 measurements. For the proposed retrieval method, 18% should be used as uncertainty for
556 RLWC from rain properties in Wu et al. (2015) and 30% for CLWC from cloud properties in
557 Dong et al. (2014a and 2014b). The actual uncertainty depends on the accuracy of merged
558 sounding data, the detectability of WACR near cloud base and the effect of entrainment on

559 cloud adiabaticity during precipitating. In the recent aircraft field campaign, the Aerosol and
560 Cloud Experiments in Eastern North Atlantic (ACE-ENA) was conducted during 2017-2018
561 with a total of 39 flights over the Azores, near the ARM ENA site on Graciosa Island. These
562 aircraft in situ measurements will be used to validate the ground-based retrievals and
563 quantitatively estimate their uncertainties in the future.

564 Figure A1 shows an example of the retrieval results. The merged sounding, ceilometer,
565 microwave radiometer, WACR and ceilometer are used in the retrieval. Whenever one or more
566 instruments are not reliable, that time step is skipped, and this results in the gaps in the CLWC
567 and RLWC as shown in Figures A1(b) and A1(c). When the cloud is classified as
568 nonprecipitating, no RLWC will be retrieved as well. Using air density (ρ_{air}) profiles
569 calculated from temperature and pressure in merged sounding, mixing ratio (q) can be
570 calculated from LWC using $q(z) = LWC(z)/\rho_{air}(z)$.

571 **Acknowledgements**

572 The ground-based measurements were obtained from the Atmospheric Radiation Measurement
573 (ARM) Program sponsored by the U.S. Department of Energy (DOE) Office of Energy
574 Research, Office of Health and Environmental Research, and Environmental Sciences
575 Division. The data can be downloaded from <http://www.archive.arm.gov/>. This research was
576 supported by the DOE CESM project under grant DE-SC0014641 at the University of Arizona

577 through subaward from University of Maryland at Baltimore County, and the NSF project
578 under grant AGS-1700728 at University of Arizona. The authors thank Dr. Yangang Liu at
579 Brookhaven National Laboratory for insightful comments and Ms. Casey E. Oswant at the
580 University of Arizona for proof reading the manuscript. The three anonymous reviewers are
581 acknowledged for constructive comments and suggestions which helped to improve the
582 manuscript.

583

584 **References**

- 585 Ahlgrim, M., and Forbes, R.: Improving the Representation of Low Clouds and Drizzle in
586 the ECMWF Model Based on ARM Observations from the Azores, *J. Clim.*, doi:
587 10.1175/MWR-D-13-00153.1, 2014.
- 588 Albrecht, B., Fairall, C., Thomson, D., White, A., Snider, J., and Schubert, W.: Surface-based
589 remote-sensing of the observed and the adiabatic liquid water-content of stratocumulus
590 clouds, *Geophys. Res. Lett.*, 17, 89–92, doi:10.1029/G1017i001p00089, 1990.
- 591 Austin, P., Wang, Y., Kujala, V., and Pincus, R.: Precipitation in Stratocumulus Clouds:
592 Observational and Modeling Results, *J. Atmos. Sci.*, 52, 2329–2352, doi:10.1175/1520-
593 0469(1995)052<2329:PISCOA>2.0.CO;2, 1995.
- 594 Bai, H., Gong, C., Wang, M., Zhang, Z., and L'Ecuyer, T.: Estimating precipitation
595 susceptibility in warm marine clouds using multi-sensor aerosol and cloud products from
596 A-Train satellites, *Atmos. Chem. Phys.*, 18, 1763-1783, [https://doi.org/10.5194/acp-18-](https://doi.org/10.5194/acp-18-1763-2018)
597 1763-2018, 2018.

598 Barker H. W., Wiellicki B.A., Parker L.: A parameterization for computing grid-averaged solar
599 fluxes for inhomogeneous marine boundary layer clouds. Part II: Validation using satellite
600 data. *J. Atmos. Sci.* 53: 2304–2316, 1996.

601 Beheng, K. D.: A parameterization of warm cloud microphysical conversion processes, *Atmos.*
602 *Res.*, 33, 193-206, 1994.

603 Bony, S., and Dufresne, J.-L.: Marine boundary layer clouds at the heart of tropical cloud
604 feedback uncertainties in climate models, *Geophys. Res. Lett.*, 32, L20806,
605 doi:10.1029/2005GL023851, 2005.

606 Boutle, I. A., Abel, S. J., Hill, P. G., and Morcrette, C. J.: Spatial variability of liquid cloud and
607 rain: Observations and microphysical effects. *Quart. J. Roy. Meteor. Soc.*, 140, 583–594,
608 doi:10.1002/qj.2140, 2014.

609 Chen, T., Rossow, W. B., and Zhang, Y.: Radiative Effects of Cloud-Type Variations, *J. Clim.*,
610 13, 264–286, 2000.

611 Cheng, A., and Xu. K.-M.: A PDF-based microphysics parameterization for simulation of
612 drizzling boundary layer clouds, *J. Atmos. Sci.*, 66, 2317–2334,
613 doi:10.1175/2009JAS2944.1, 2009.

614 Comstock, K. K., Yuter, S. E., Wood, R., and Bretherton, C. S.: The Three-Dimensional
615 Structure and Kinematics of Drizzling Stratocumulus, *Mon. Weather Rev.*, 135, 3767–
616 3784, doi:10.1175/2007MWR1944.1, 2007.

617 Dong X., Ackerman, T. P., and Clothiaux, E. E.: Parameterizations of Microphysical and
618 Radiative Properties of Boundary Layer Stratus from Ground-based measurements, *J.*
619 *Geophys. Res.*, 102, 31,681-31,393, 1998.

620 Dong, X., Minnis, P., Ackerman, T. P., Clothiaux, E. E., Mace, G. G., Long, C. N., and
621 Liljegren, J. C.: A 25-month database of stratus cloud properties generated from ground-
622 based measurements at the ARM SGP site, *J. Geophys. Res.*, 105, 4529-4538, 2000.

623 Dong, X., Xi, B., Kennedy, A., Minnis, P. and Wood, R.: A 19-month Marine Aerosol-
624 Cloud_Radiation Properties derived from DOE ARM AMF deployment at the Azores:
625 Part I: Cloud Fraction and Single-layered MBL cloud Properties, *J. Clim.*, 27,
626 doi:10.1175/JCLI-D-13-00553.1, 2014a.

627 Dong, X., Xi, B., and Wu, P.: Investigation of Diurnal Variation of MBL Cloud Microphysical
628 Properties at the Azores, *J. Clim.*, 27, 8827-8835, 2014b.

629 Fielding, M. D., Chiu, J. C., Hogan, R. J., Feingold, G., Eloranta, E., O'Connor, E. J. and
630 Cadeddu, M. P.: Joint retrievals of cloud and drizzle in marine boundary layer clouds using
631 ground-based radar, lidar and zenith radiances. *Atmospheric Measurement Techniques*, 8,
632 pp. 2663-2683. ISSN 1867-8548 doi: 10.5194/amt-8-2663-2015, 2015.

633 Frisch, A., Fairall, C., and Snider, J.: Measurement of stratus cloud and drizzle parameters in
634 ASTEX with a Ka-band Doppler radar and a microwave radiometer, *J. Atmos. Sci.*, 52,
635 2788–2799, 1995.

636 Geoffroy, O., Brenguier, J.-L., and Burnet, F.: Parametric representation of the cloud droplet
637 spectra for LES warm bulk microphysical schemes, *Atmos. Chem. Phys.*, 10, 4835-4848,
638 <https://doi.org/10.5194/acp-10-4835-2010>, 2010.

639 Hahn, C. and Warren, S.: A gridded climatology of clouds over land (1971–96) and ocean
640 (1954–97) from surface observations worldwide, Numeric Data Package NDP-026E
641 ORNL/CDIAC-153, CDIAC, Department of Energy, Oak Ridge, Tennessee, 2007.

642 Hartmann, D. L., Ockert-Bell, M. E., and Michelsen, M. L.: The Effect of Cloud Type on
643 Earth's Energy Balance: Global Analysis, *J. Climate*, 5, 1281–1304,
644 [https://doi.org/10.1175/15200442\(1992\)005<1281:TEOCTO>2.0.CO;2](https://doi.org/10.1175/15200442(1992)005<1281:TEOCTO>2.0.CO;2), 1992.

645 Hartmann, D. L. and Short, D. A.: On the use of earth radiation budget statistics for studies of
646 clouds and climate, *J. Atmos. Sci.*, 37, 1233–1250, doi:10.1175/1520-
647 0469(1980)037<1233:OTUOER>2.0.CO;2, 1980.

648 Hill, P. G., Morcrette, C. J., and Boutle, I. A.: A regime-dependent parametrization of subgrid-
649 scale cloud water content variability, *Q. J. R. Meteorol. Soc.*, 141, 1975–1986, 2015.

650 Houghton, J. T., Ding, Y., Griggs, D.J., Noguer, M., van der Linden, P.J., Dai, X., Maskell, K.,
651 and Johnson, C.A.: *Climate Change: The Scientific Basis*, Cambridge University Press,
652 881 pp, 2001.

653 Jess, S.: Impact of subgrid variability on large-scale precipitation formation in the climate
654 model ECHAM5, PhD thesis, Dep. of Environ. Syst. Sci., ETH Zurich, Zurich,
655 Switzerland, 2010.

656 Jiang, J., Su, H., Zhai, C., Perun, V. S., Del Genio, A., Nazarenko, L. S., Donner, L. J.,
657 Horowitz, Seman, L., Cole, C., J., Gettelman, A., Ringer, M. A., Rotstayn, L., Jeffrey, S.,
658 Wu, T., Brient, F., Dufresne, J-L., Kawai, H., Koshiro, T., Watanabe, M., LÉcuyer, T. S.,
659 Volodin, E. M., Iversen, Drange, T., H., Mesquita, M. D. S., Read, W. G., Waters, J. W.,
660 Tian, B., Teixeira, J., and Stephens, G. L.: Evaluation of cloud and water vapor simulations
661 in CMIP5 climate models using NASA “A-train” satellite observations, *J. Geophys. Res.*,
662 117, D14105, doi:10.1029/2011JD017237, 2012.

663 Kessler, E.: On the distribution and continuity of water substance in atmospheric circulations,
664 *Met. Monograph* 10, No. 32, American Meteorological Society, Boston, USA, 84 pp.,
665 1969.

666 Khairoutdinov, M. and Kogan, Y.: A New Cloud Physics Parameterization in a Large-Eddy
667 Simulation Model of Marine Stratocumulus, *Mon. Wea. Rev.*, 128, 229-243, 2000.

668 Kooperman, G. J., Pritchard, M. S., Ghan, S. J., Wang, M., Somerville, R. C., and Russell, L.
669 M.: Constraining the influence of natural variability to improve estimates of global aerosol
670 indirect effects in a nudged version of the Community Atmosphere Model 5, *J. Geophys.*
671 *Res.*, 117, D23204, <https://doi.org/10.1029/2012JD018588>, 2012.

672 Kubar, T. L., Hartmann, D. L., and Wood, R.: Understanding the importance of microphysics
673 and macrophysics in marine low clouds, Part I: satellite observations. *J. Atmos. Sci.*, 66,
674 2953-2972, doi: 10.1175/2009JAS3071.1, 2009.

675 Larson, V. E., Nielsen, B. J., Fan, J., and Ovchinnikov, M.: Parameterizing correlations
676 between hydrometeor species in mixed-phase Arctic clouds, *J. Geophys. Res.*, 116,
677 D00T02, doi:10.1029/2010JD015570, 2011.

678 Larson, V. E., and Griffin, B. M.: Analytic upscaling of a local microphysics scheme. Part I:
679 Derivation. *Quart. J. Roy. Meteor. Soc.*, 139, 46–57, 2013.

680 Lebsock, M. D., Morrison, H., and Gettelman, A.: Microphysical implications of cloud-
681 precipitation covariance derived from satellite remote sensing, *J. Geophys. Res.-Atmos.*,
682 118, 6521–6533, <https://doi.org/10.1002/jgrd.50347>, 2013.

683 Lee, H., and Baik, J.-J.: A physically based autoconversion parameterization. *Journal of the*
684 *Atmospheric Sciences*, 74, 1599–1616, 2017.

685 Leon, D. C., Wang, Z., and Liu, D.: Climatology of drizzle in marine boundary layer clouds
686 based on 1 year of data from CloudSat and Cloud-Aerosol Lidar and Infrared Pathfinder
687 Satellite Observations (CALIPSO), *J. Geophys. Res.*, 113, D00A14,
688 doi:10.1029/2008JD009835, 2008.

689 Liljegren, J. C., Clothiaux, E. E., Mace, G. G., Kato, S., and Dong, X.: A new retrieval for
690 cloud liquid water path using a ground-based microwave radiometer and measurements of
691 cloud temperature, *J. Geophys. Res.*, 106, 14,485-14,500, 2001.

692 Liu, Y. and Daum, P. H.: Parameterization of the autoconversion process, Part I: Analytical
693 formulation of the Kessler-type parameterizations, *J. Atmos. Sci.*, 61, 1539–1548, 2004.

694 Liu, Y., Daum, P. H., and McGraw, R.: Parameterization of the autoconversion process. Part
695 II: Generalization of Sundqvist-type parameterizations, *J. Atmos. Sci.*, 63, 1103–1109,
696 2006a.

697 Liu, Y., Daum, P. H., McGraw, R., Miller, M.: Generalized threshold function accounting for
698 effect of relative dispersion on threshold behavior of autoconversion process. *Geophys.*
699 *Res. Lett.*, 33, L11804, 2006b.

700 Michibata, T., and Takemura, T.: Evaluation of autoconversion schemes in a single model
701 framework with satellite observations, *J. Geophys. Res. Atmos.*, 120, 9570–9590,
702 doi:10.1002/2015JD023818, 2015.

703 Miles, N. L., Verlinde, J., and Clothiaux, E. E.: Cloud-droplet size distributions in low-level
704 stratiform clouds. *J. Atmos. Sci.*, 57, 295–311, doi:10.1175/1520-0469(2000)057,
705 0295:CDS DIL.2.0.CO;2, 2000.

706 Morrison, H. and Gettelman, A.: A new two-moment bulk stratiform cloud microphysics
707 scheme in the Community Atmosphere Model, version 3 (CAM3). Part I: Description and
708 numerical tests, *J. Climate*, 21, 3642–3659, 2008.

709 Nam, C., and Quaas, J.: Evaluation of clouds and precipitation in the ECHAM5 general
710 circulation model using CALIPSO and CloudSat satellite data, *J. Clim.*, 25, 4975–4992,
711 doi:10.1175/JCLI-D-11-00347.1, 2012.

712 O’Connor, E. J., Hogan, R. J., and Illingworth, A. J.: Retrieving stratocumulus drizzle
713 parameters using Doppler radar and lidar, *J. of Applied Meteorol.*, 44, 14-27, 2005.

714 Pincus, R., McFarlane, S. A., and Klein, S. A.: Albedo bias and the horizontal variability of
715 clouds in subtropical marine boundary layers: Observations from ships and satellites, *J.*
716 *Geophys. Res.*, 104, 6183–6191, doi:10.1029/1998JD200125, 1999.

717 Pincus, R., and Klein, S. A.: Unresolved spatial variability and microphysical process rates in
718 large-scale models. *J. Geophys. Res.*, 105D, 27 059–27 065, 2000.

719 Quaas, J., Ming, Y., Menon, S., Takemura, T., Wang, M., Penner, J. E., Gettelman, A.,
720 Lohmann, U., Bellouin, N., Boucher, O., Sayer, A. M., Thomas, G. E., McComiskey, A.,
721 Feingold, G., Hoose, C., Kristjánsson, J. E., Liu, X., Balkanski, Y., Donner, L. J., Ginoux,
722 P. A., Stier, P., Grandey, B., Feichter, J., Sednev, Bauer, S. E., Koch, D., Grainger, R. G.,

723 Kirkevåg, A., Iversen, T., Seland, Ø., Easter, R., Ghan, S. J., Rasch, P. J., Morrison, H.,
724 Lamarque, J.-F., Iacono, M. J., Kinne, S., and Schulz, M.: Aerosol indirect effects –
725 general circulation model intercomparison and evaluation with satellite data, *Atmos.*
726 *Chem. Phys.*, 9, 8697–8717, <https://doi.org/10.5194/acp-9-8697-2009>, 2009.

727 Randall, D. A., Coakley, J. A., Fairall, C. W., Knopfli, R. A., and Lenschow, D. H.: Outlook
728 for research on marine subtropical stratocumulus clouds. *Bull. Amer. Meteor. Soc.*, 65,
729 1290–1301, 1984.

730 Rémillard, J., Kollias, P., Luke, E., and Wood, R.: Marine Boundary Layer Cloud Observations
731 in the Azores, *J. Climate*, 25, 7381–7398, doi: [http://dx.doi.org/10.1175/JCLI-D-11-](http://dx.doi.org/10.1175/JCLI-D-11-00610.1)
732 00610.1, 2012.

733 Rémillard, J., Kollias, P., and Szyrmer, W.: Radar-radiometer re-
734 trievals of cloud number concentration and dispersion parameter in nondrizzling marine stratocumulus, *Atmos.*
735 *Meas. Tech.*, 6, 1817–1828, doi:10.5194/amt-6-1817-2013, 2013.

736 Slingo, A.: Sensitivity of the Earth’s radiation budget to changes in low clouds, *Nature*, 343,
737 49–51, <https://doi.org/10.1038/343049a0>, 1990.

738 Song, H., Zhang, Z., Ma, P.-L., Ghan, S. J., and Wang, M.: An Evaluation of Marine Boundary
739 Layer Cloud Property Simulations in the Community Atmosphere Model Using Satellite
740 Observations: Conventional Subgrid Parameterization versus CLUBB, *J. Clim.*,
741 doi:10.1175/JCLI-D-17-0277.1, 2018.

742 Stanfield, R., Dong, X., Xi, B., Gel Genio, A., Minnis, P., and Jiang, J.: Assessment of NASA
743 GISS CMIP5 and post CMIP5 Simulated Clouds and TOA Radiation Budgets Using
744 Satellite Observations: Part I: Cloud Fraction and Properties, *J. Clim.*, doi:10.1175/JCLI-
745 D-13-00588.1, 2014.

746 Tripoli, G. J. and Cotton, W. R.: A numerical investigation of several factors contributing to
747 the observed variable intensity of deep convection over South Florida., *J. Appl. Meteorol.*,
748 19, 1037–1063, 1980.

749 Troyan, D.: Merged Sounding Value-Added Product, Tech. Rep., DOE/SC-ARM/TR-087,
750 2012.

751 Walters, D., Baran, A., Boutle, I., Brooks, M., Earnshaw, P., Edwards, J., Furtado, K., Hill, P.,
752 Lock, A., Manners, J., Morcrette, C., Mulcahy, J., Sanchez, C., Smith, C., Stratton, R.,
753 Tennant, W., Tomassini, L., van Weverberg, K., Vosper, S., Willett, M., Browse, J.,
754 Bushell, A., Dalvi, M., Essery, R., Gedney, N., Hardiman, S., Johnson, B., Johnson, C.,
755 Jones, A., Mann, G., Milton, S., Rumbold, H., Sellar, A., Ujiie, M., Whittall, M., Williams,
756 K. and Zerroukat, M. The Met Office Unified Model Global Atmosphere 7.0/7.1 and
757 JULES Global Land 7.0 configurations. *Geosci. Model Dev.*, doi:10.5194/gmd-2017-291,
758 2017.

759 Wang, M., Ghan, S., Liu, X., L'Ecuyer, T. S., Zhang, K., Morrison, H., Ovchinnikov, M.,
760 Easter, R., Marchand, R., Chand, D., Qian, Y., and Penner, J. E.: Constraining cloud
761 lifetime effects of aerosols using A-Train satellite observations, *Geophys. Res. Lett.*, 39,
762 L15709, <https://doi.org/10.1029/2012GL052204>, 2012.

763 Warren, S. G., Hahn, C. J., London, J., Chervin, R. M., and Jenne, R.: Global distribution of
764 total cloud cover and cloud type amount over land, Tech. Rep. Tech. Note TN-317 STR,
765 NCAR, 1986.

766 Warren, S. G., Hahn, C. J., London, J., Chervin, R. M., and Jenne, R.: Global distribution of
767 total cloud cover and cloud type amount over land, Tech. Rep. Tech. Note TN-317 STR,
768 NCAR, 1988.

769 Weber, T., and Quaas, J.: Incorporating the subgrid-scale variability of clouds in the
770 autoconversion parameterization using a PDF-scheme, *J. Adv. Model. Earth Syst.*, 4,
771 M11003, doi:10.1029/2012MS000156, 2012.

772 Wielicki, B. A., Cess, R. D., King, M. D., Randall, D. A., and Harrison, E. F.: Mission to planet
773 Earth: Role of clouds and radiation in climate, *Bull. Amer. Meteor. Soc.*, 76, 2125–2153,
774 doi:10.1175/1520-0477(1995)076<2125:MTPERO.2.0.CO;2, 1995.

775 Witte, M. K., Yuan, T., Chuang, P. Y., Platnick, S., Meyer, K. G., Wind, G., and Jonsson, H.
776 H.: MODIS retrievals of cloud effective radius in marine stratocumulus exhibit no
777 significant bias. *Geophysical Research Letters*, 45, 10,656–10,664.
778 <https://doi.org/10.1029/2018GL079325>, 2018.

779 Wood, R., Field, P. R., and Cotton, W. R.: Autoconversion rate bias in stratiform boundary
780 layer cloud parameterization. *Atmos. Res.*, 65, 109–128, 2002.

781 Wood, R.: Drizzle in stratiform boundary layer clouds. Part I: Vertical and horizontal structure,
782 *J. Atmos. Sci.*, 62, 3011–3033, 2005a.

783 Wood, R.: Drizzle in stratiform boundary layer clouds. Part II: Microphysical aspects, J.
784 *Atmos. Sci.*, 62, 3034–3050, 2005b.

785 Wood, R. and Hartmann, D.: Spatial variability of liquid water path in marine low cloud: The
786 importance of mesoscale cellular convection, *J. Climate*, 19, 1748–1764, 2006.

787 Wood, R.: Cancellation of aerosol indirect effects in marine stratocumulus through cloud
788 thinning. *J. Atmos. Sci.*, 64, 2657–2669, 2007.

789 Wood, R.: Stratocumulus Clouds, *Mon. Wea. Rev.*, 140, 2373–2423. doi:
790 <http://dx.doi.org/10.1175/MWR-D-11-00121.1>, 2012.

791 Wood, R., Wyant, M., Bretherton, C. S., Rémillard, J., Kollias, P., Fletcher, J., Stemmler, J.,
792 deSzoeko, S., Yuter, S., Miller, M., Mechem, D., Tselioudis, G., Chiu, C., Mann, J.,
793 O'Connor, E., Hogan, R., Dong, X., Miller, M., Ghate, V., Jefferson, A., Min, Q., Minnis,
794 P., Palinkonda, R., Albrecht, B., Luke, E., Hannay, C., Lin, Y.: Clouds, Aerosol, and
795 Precipitation in the Marine Boundary Layer: An ARM Mobile Facility Deployment, *Bull.*
796 *Amer. Meteorol. Soc.*, doi: <http://dx.doi.org/10.1175/BAMS-D-13-00180.1>, 2015.

797 Wu, P., Dong, X. and Xi, B.: Marine boundary layer drizzle properties and their impact on
798 cloud property retrieval, *Atmos. Meas. Tech.*, 8, 3555–3562. doi: 10.5194/amt-8-3555-
799 2015, 2015.

800 Wu, P., Dong, X., Xi, B., Liu, Y., Thieman, M., and Minnis, P.: Effects of environment forcing
801 on marine boundary layer cloud-drizzle processes, *J. Geophys. Res. Atmos.*, 122, 4463–
802 4478, doi:10.1002/2016JD026326, 2017.

803 Xie, X., and Zhang, M.: Scale-aware parameterization of liquid cloud inhomogeneity and its
804 impact on simulated climate in CESM, *J. Geophys. Res. Atmos.*, 120, 8359–8371,
805 doi:10.1002/2015JD023565, 2015.

806 Yoo, H., and Li, Z.: Evaluation of cloud properties in the NOAA/NCEP Global Forecast
807 System using multiple satellite products. *Climate Dyn.*, 39, 2769–2787,
808 doi:10.1007/s00382-012-1430-0, 2012.

809 Yoo, H., and Li, Z., Hou, Y.-T., Lord, S., Weng, F., and Barker, H. W.: Diagnosis and testing
810 of low-level cloud parameterizations for the NCEP/GFS using satellite and ground-based
811 measurements. *Climate Dyn.*, 41, 1595–1613, doi:10.1007/s00382-013-1884-8, 2013.

812 Zhang, J., Lohmann, U., and Lin, B.: A new statistically based autoconversion rate
813 parameterization for use in large-scale models. *J. Geophys. Res.*, 107, 4750,
814 doi:10.1029/2001JD001484, 2002.

815 Zhang, Z., Song, H., Ma, P.-L., Larson, V., Wang, M., Dong, X., and Wang, J.: Subgrid
816 variations of cloud water and droplet number concentration over tropical oceans: satellite
817 observations and implications for warm rain simulation in climate models. Submitted to
818 *Atmos. Chem. Phys.*, 2018.

819

820 **Table 1. The parameters of autoconversion and accretion formulations for four**
 821 **parameterizations.**

822

	A	$a1$	$a2$	B	b
Khairoutdinov and Kogan (2000)	1350	2.47	-1.79	67	1.15
	$1.3 \times 10\beta_6^6$,				
	where $\beta_6^6 = [(r_v + 3)/r_v]^2$,				
Liu and Daum (2004)	r_v is mean volume radius.	3	-1	N/A	N/A
	modification was made by Wood (2005b)				
Tripoli and Cotton (1980)	3268	7/3	-1/3	1	1
Beheng (1994)	3×10^{34} for $N_c < 200 \text{ cm}^{-3}$ 9.9 for $N_c > 200 \text{ cm}^{-3}$	4.7	-3.3	1	1

823

824 **Table 2. Autoconversion (left) and accretion (right) enhancement factors in different**
 825 **boundary layer conditions (LTS > 18 K for stable, LTS < 13.5 K for unstable and LTS**
 826 **within 13.5 and 18 K for mid-stable) and in different LWP regimes (LWP ≤ 75 g m⁻² for**
 827 **non-precipitating and LWP > 75 g m⁻² for precipitating).**

828

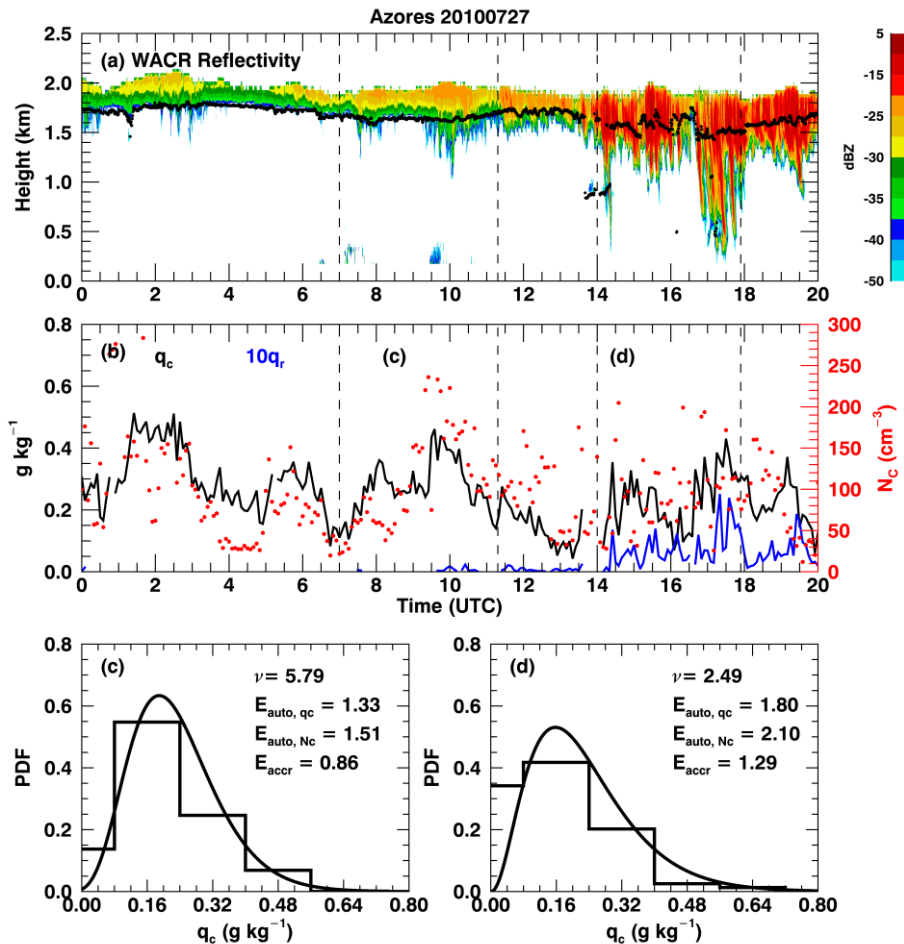
	LWP ≤ 75 g m ⁻²	LWP > 75 g m ⁻²
LTS > 18 K	2.32/1.42	2.75/1.52
13.5 ≤ LTS ≤ 18K	2.61/1.47	3.07/1.68
LTS < 13.5 K	4.62/1.72	6.94/1.86

829

830 **Table 3. Autoconversion and accretion enhancement factors (E_{auto} and E_{accr}) for the**
 831 **parameterizations in Table 1 except the Khairoutdinov and Kogan (2000) scheme. The**
 832 **values are averaged for 60-km and 180-km equivalent sizes.**
 833

	E_{auto}		E_{accr}	
	60-km	180-km	60-km	180-km
Liu and Daum (2004)	3.82	4.23	N/A	N/A
Tripoli and Cotton (1980)	2.46	2.69	1.47	1.56
Beheng (1994)	6.94	5.88	1.47	1.56

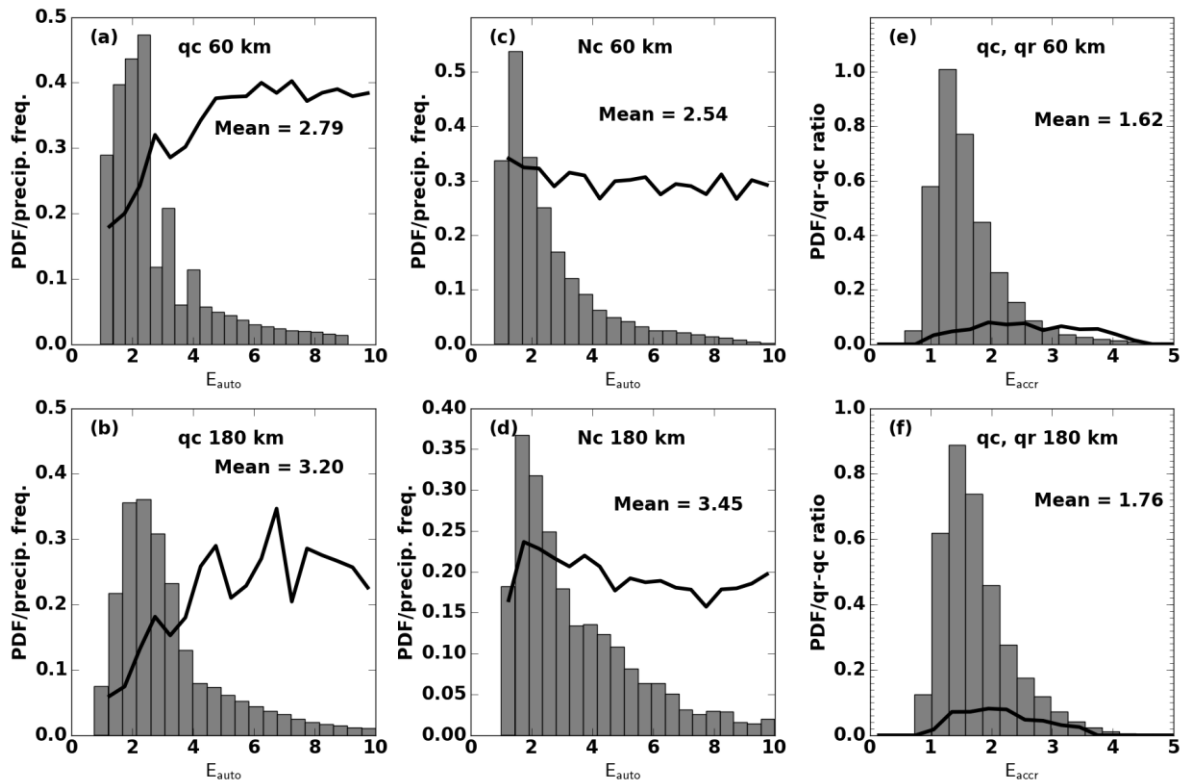
834



835

836 **Figure 1. Observations and retrievals over Azores on 27 July 2010. (a) W-band ARM**
 837 **cloud radar (WACR) reflectivity (contour) superimposed with cloud-base height (black**
 838 **dots). (b) Black line represents averaged cloud water mixing ratio (q_c) within the top five**
 839 **range gates, blue line represents averaged rain ($\times 10$) water mixing ratio within five range**
 840 **gates around maximum reflectivity, red dots are the retrieved cloud droplet number**
 841 **concentration (N_c). Dashed lines represent two periods that have 60 km equivalent sizes**
 842 **with similar \bar{q}_c but different distributions as shown by step lines in (c) and (d). Curved**
 843 **lines in (c) and (d) are fitted gamma distributions with the corresponding shape**
 844 **parameter (ν) shown on the upper right. N_c distributions are not shown. The calculated**
 845 **autoconversion (E_{auto, q_c} from q_c and E_{auto, N_c} from N_c) and accretion (E_{accr}) enhancement**
 846 **factors are also shown.**

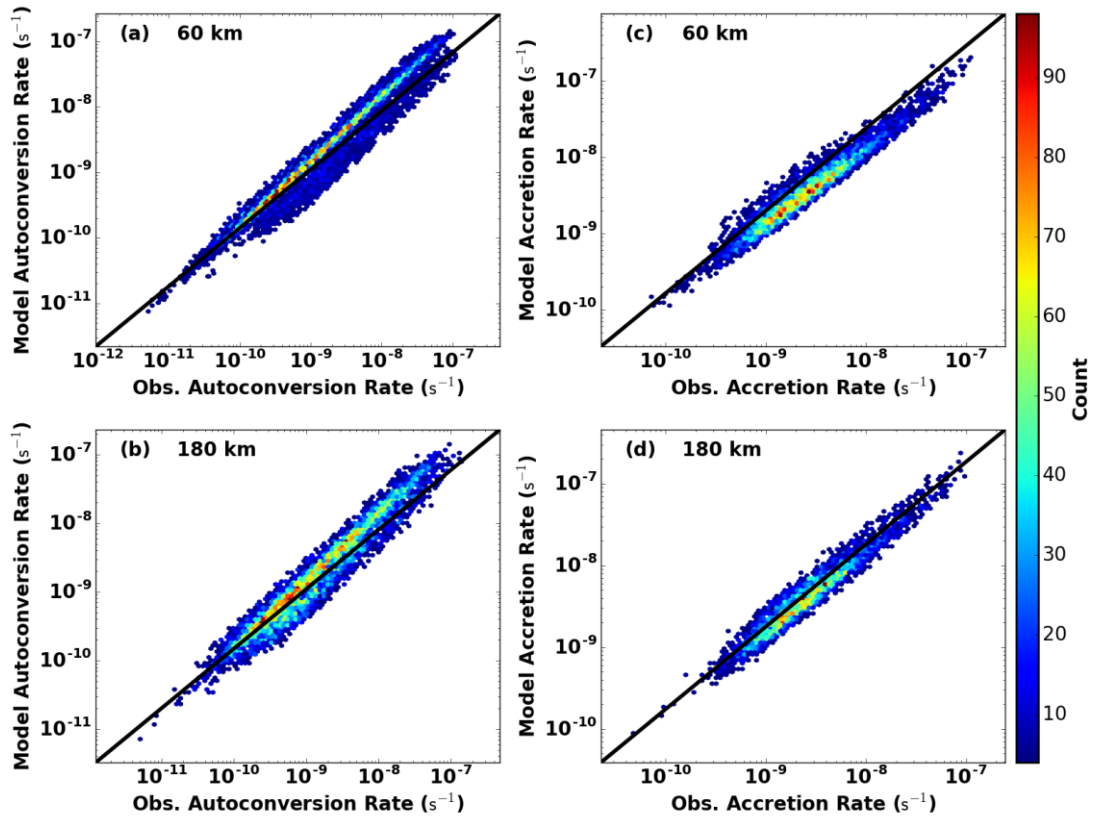
847
848



849

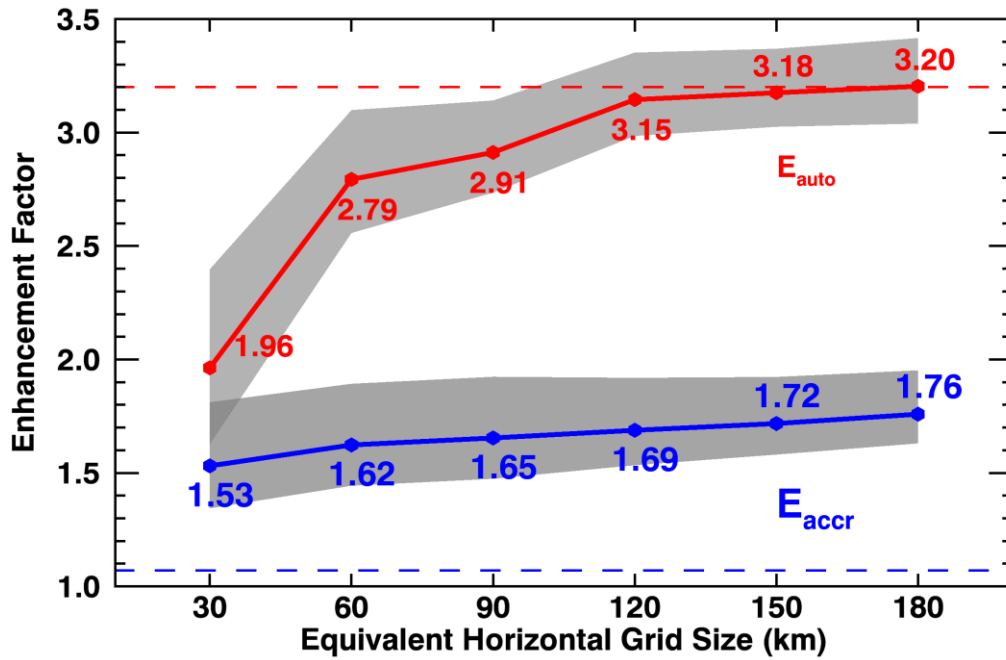
850 **Figure 2. Probability density functions (PDFs) of autoconversion (a - d) and accretion (e**
851 **- f) enhancement factors calculated from q_c (a-b), N_c (c-d), and the covariance of q_c and**
852 **q_r (e-f). The two rows show the results from 60-km and 180-km equivalent sizes,**
853 **respectively, with their average values. Black lines represent precipitation frequency in**
854 **each bin in (a)-(d) and the ratio of layer-mean q_r to q_c in (e)-(f).**

855



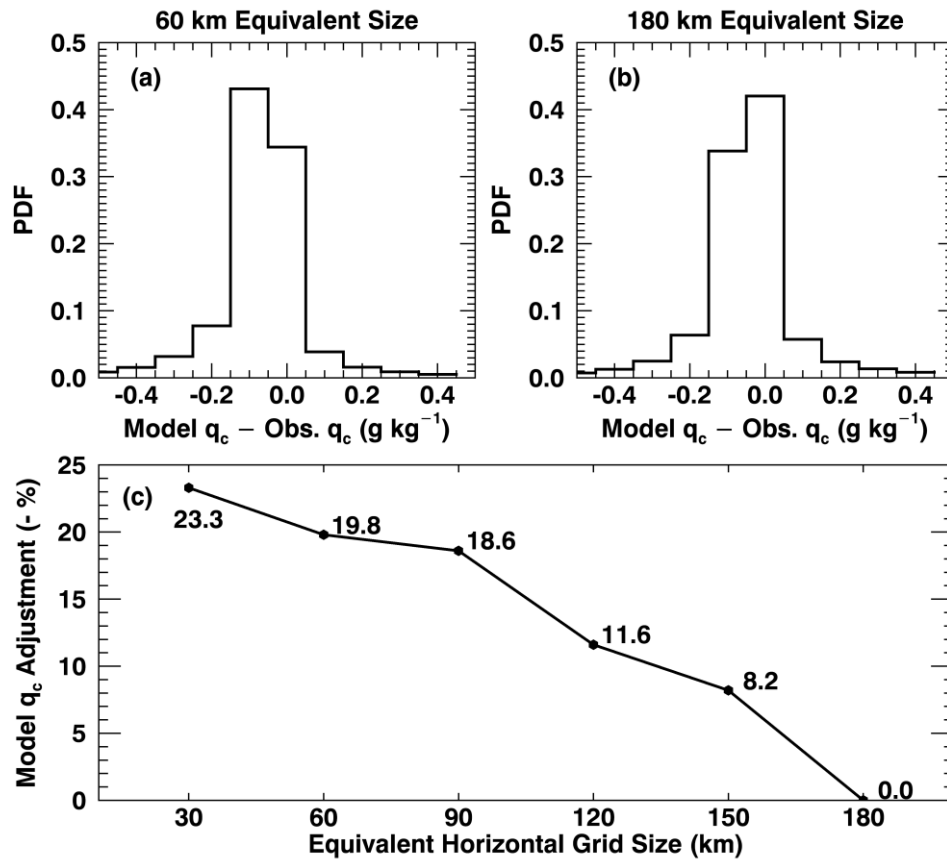
856

857 **Figure 3.** Comparison of autoconversion (a-b) and accretion (c-d) rates derived from
 858 observations (x-axis) and from model (y-axis). Results are for 60-km (a and c) and 180-
 859 km model equivalent sizes. Colored dots represent joint number densities.



861 **Figure 4. Autoconversion (red line) and accretion (blue line) enhancement factors as a**
 862 **function of equivalent sizes. The shaded areas are calculated by varying q_c and q_r within**
 863 **their retrieval uncertainties. The two dashed lines show the constant values of**
 864 **autoconversion (3.2) and accretion (1.07) enhancement factors prescribed in MG08.**

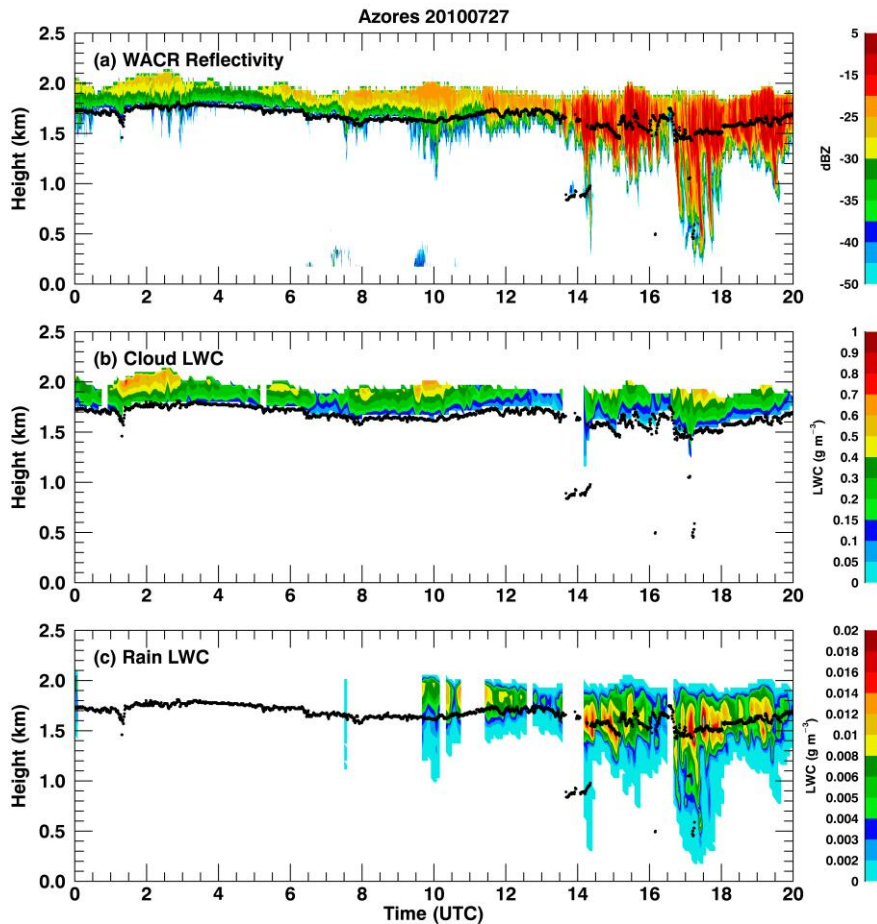
865



866

867 **Figure 5. q_c needed for models to adjust to reach the same autoconversion rate as**
 868 **observations for (a) 60-km and (b) 180-km model equivalent sizes. Positive biases**
 869 **represent increased q_c are required in models and negative biases mean decreased q_c . The**
 870 **average percentages of adjustments for different equivalent sizes are shown in panel (c)**
 871 **and note that the percentages in the vertical axis are negative.**

872



873

874 **Figure A1. Joint retrieval of cloud and rain liquid water content (CLWC and RLWC) for**
 875 **the same case as in Figure 1. (a) WACR reflectivity, (b) CLWC, and (c) RLWC. The black**
 876 **dots represent cloud base height. Blank gaps are due to the data from one or more**
 877 **observations are not available or reliable. For example, the gap before 14 UTC is due to**
 878 **multiple cloud layers are detected whereas we only focus on single layer cloud.**